Supplementary Materials for
Intrinsic transverse magnetic nonreciprocal response in a noncollinear antiferromagnet

Hengrui Gui[1†], Ziming Wang[1,2†], Zekai Shi[1], Jiawen Zhang[1], Yongjian Li[1], Ke Xia[3], Yu Liu[1],
Jinglei Zhang[4], Taishi Chen[3*], Huiqiu Yuan[1,5,6*], Lun-Hui Hu[1*], Lin Jiao[1*],

*Corresponding author. Email: chentaishi@seu.edu.cn; hqyuan@zju.edu.cn; lunhui@zju.edu.cn;
lin.jiao@zju.edu.cn

†These authors contributed equally to this work.

Materials and Methods

Bulk Mn_3Ge single crystals were synthesized utilizing a high-throughput bismuth (Bi) flux method (*58*). As illustrated in Fig. S1, the as-grown crystals exhibit either hexagonal plate-like or elongated strip-like morphologies, contingent upon the initial Bi:Mn:Ge molar ratios. Surface impurities were eliminated via chemical etching in a dilute nitric acid solution (2.5% v/v). Powder X-ray diffraction (XRD) analysis (Fig. S2(a)) demonstrates the efficacy of this etching process in removing residual surface flux. And the temperature dependence of XRD result (Fig. S2(b)) shows that there is no structural phase transition when cooling Mn_3Ge across 210 K.

Crystallographic orientations were further confirmed by combining single-crystal XRD with Laue back-reflection patterns (Fig. S3). For the strip-like samples, the elongation axis corresponds to the [0001], with the broad surface identified as the $[2\bar{1}\bar{1}0]$ plane. For hexagonal platelets, it is confirmed that the basal plane is [0001], with the vector connecting the center to the edge vertex aligned along the $[0\bar{1}\bar{1}0]$ direction.

The quality of our flux-grown single crystals has a significant improvement over previously reported bulk samples, evidenced by the following key characteristics: 1. Stoichiometric precision: Energy-dispersive X-ray spectroscopy (EDS) combined with scanning electron microscopy (SEM) reveals that the Mn:Ge molar ratio is strictly maintained at 3:1 across the scanned areas (Fig. S4), indicating high chemical homogeneity. 2. Magnetization measurements (Fig. S5(a)) demonstrate a vanishing remanent magnetization along the [0001] direction (perpendicular to the kagome plane), while a weak ferromagnetic signal persists within the kagome plane (Fig. S5(b)).

These findings indicate not only a negligible concentration of defects in our sample—such as excess magnetic Mn, Mn vacancies, or Mn-Ge site disorder—but also, crucially, that the Mn magnetic moments are strictly confined within the kagome plane. This high degree of magnetic confinement is pivotal for elucidating the intrinsic origin of weak ferromagnetism in non-collinear antiferromagnets Mn_3X (X = Sn, Ge, Ga) and for enabling the efficient manipulation of magnetic octupole domains. Furthermore, the temperature-dependent magnetization (M-T) curves (Fig. S6) corroborate these observations. While literature suggests that excess Mn can elevate the Néel temperature (T_N) up to 380 K (*42, 43*), our crystals show a T_N of 370 K. This value is consistent with the stoichiometric limit, providing further evidence of the absence of magnetic Mn excess in our samples.

Torque magnetometry measures magnetic torque by converting a cantilever's mechanical deflection into a precise electrical signal. When an external magnetic field exerts torque on a mounted sample, the cantilever bends, which changes the electrical resistance of its embedded piezoresistors. These piezoresistors are arranged in a Wheatstone bridge circuit that translates this resistance change into a differential voltage. A lock-in amplifier is then used to measure this voltage, effectively filtering out background noise to deliver a highly sensitive signal that is directly proportional to the applied magnetic torque.

Supplementary Text

Exclude domain wall effect

Previous report by L.C. Xu et al., reported PHE in Mn_3Ge, which was attributed to the memory of antiferromagnetic domain walls (*55*). The main evidence for chiral domain wall induced PHE are: 1. the PHE appears just at T_N together with the formation of domain walls. 2. the PHE is sensitive to field training/cycle: a prior field (H_p) was applied to y-axis and then rotated to $-x$ or $+x$ axis, depending on the strength of H_p, the PHE could be very different. For example, PHE decreases with increasing H_p and is negligible for H_p above 0.8 T. 3. Moreover, the sign of the PHE value showed a well-defined memory effect controlled by the prior orientation of H_p and its history. 4. The ratio between AHE and PHE is scalable with magnetization of the sample as indicated by the authors. In principle, no nonreciprocal torque response could be induced by domain walls, as the randomly distributed/orientated domain walls could hardly contribute to a sufficient thermodynamic signal.

While the nonreciprocal torque response and PHE observed in this work occur only far below T_N, to further exclude chiral domain wall effect, we conducted a systematic memory effect test and found the observations are independent of H_p training, i.e. no memory effect. Our main results are present in Figs. S7 and S8. 1. At 300 K, we could not detect the symmetric component of ρ^{xz} despite the strength of H_p, indicating negligible PHE which is irrelevant to H_p. 2. Figure S8 test memory effect at 10 K when PHE appears. A large training field (H_p = 5 T) was applied to $-y$/$+y$-axis before rotating anticlockwise/clockwise to $+x$-axis for Hall effect measurements. The results in Fig. S8(b) show no sign change of ρ_{PHE}, which is in contrast to previous observations in

Ref. (*55*). 3. In addition, our main text shows that $\mathrm{Ratio}_{\mathrm{PHE/AHE}}$ is irrelevant to the magnetization of Mn_3Ge. Moreover, Fig. S9 presents a full data set of angular dependent torque measurements. This result demonstrates the specific directional dependence of our non-reciprocal measurements, which does not exist in the chiral domain wall scenario. Taken together, our nonreciprocal torque results and PHE are intrinsic bulk response and are distinct from chiral domain wall induced effect.

The following Tab. S1 summarizes the fact to distinguish between domain wall induced PHE and intrinsic PHE from nonreciprocal magnetic response.

Symmetry analysis of three-orbital chiral AFM

To understand the anisotropic magnetization in Mn_3X materials, we begin with a kagome lattice exhibiting coplanar antiferromagnetic order, where the magnetic configuration can adopt either left-handed or right-handed chirality. Figure S10(a) illustrates the right-handed and left-handed chiral antiferromagnetic configuration with $\kappa = \pm 1$, respectively, where the vector spin chirality is defined as

$$\kappa = \tfrac{2\sqrt{3}}{3}(\mathbf{n}_{\mathrm{A}} \times \mathbf{n}_{\mathrm{B}} + \mathbf{n}_{\mathrm{B}} \times \mathbf{n}_{\mathrm{C}} + \mathbf{n}_{\mathrm{C}} \times \mathbf{n}_{\mathrm{A}}) \cdot \hat{z}, \tag{S1}$$

where $\mathbf{n}_i$ denotes the spin orientation on the three Mn sublattices A, B, and C within the kagome unit cell. In the absence of spin-orbit coupling, the spin and orbital degrees of freedom are decoupled, and the symmetries of this antiferromagnet exhibiting two distinct chiralities can be captured by spin space group $P^{3z}6_3/{}^1m^2m^2c^m1$ (*20, 23*). Under this spin space group, the anisotropic magnetization must vanish. For instance, the threefold rotational symmetry $\{\mathcal{U}_{3z}||\mathcal{R}_{6_3z}\}$ and the combine symmetry $\{\mathcal{U}_{2z}||\mathcal{R}_{2_1z}\}\mathcal{T}$ constrain the magnetization vector $\mathbf{M} = (M^x, M^y, M^z)$ to be $\mathbf{M} = (0, 0, 0)$, where $\mathcal{T}$ is time-reversal symmetry, $\mathcal{U}_n$ and $\mathcal{R}_n$ are the rotational symmetry operators in spin and lattice subspace, respectively. The subscript $n_{n/2}$ on $\mathcal{R}_{n_{n/2}}$ marks a n-fold screw axis.

In fact, spin-orbit coupling can no longer be considered negligible in semimetal materials such as Mn_3Sn and Mn_3Ge. Its interplay with non-collinear antiferromagnetic orders breaks the spin space symmetries, necessitating a description within the magnetic group framework. Here, the right-handed and left-handed chiral antiferromagnet are distinguished by the magnetic space group $P6_3'$ and $P2_1'$, respectively. For the right-handed system, the combine symmetry $C_{6_3z}\mathcal{T}$ constrain magnetization vector $\mathbf{M} = (0, 0, 0)$, where C_n is the magnetic rotational symmetry. For the left-handed system, the symmetry $C_{2_1z}\mathcal{T}$ forces $M^z = 0$ but imposes no constrain on M^x or M^y.

In particular, the right-handed and left-handed chiral antiferromagnets correspond to the magnetic space group $P6_3'22'$ and $P2_1'2'2$, respectively, with $\mathbf{n}_\mathrm{C}$ oriented $\mathbf{n}_\mathrm{C} = \pm\frac{\mathbf{a}_1+\mathbf{a}_2}{2\sqrt{3}a}$ or $\pm\frac{\mathbf{a}_1-\mathbf{a}_2}{2a}$ ($\mathbf{n}_\mathrm{C} = -\frac{\mathbf{a}_1+\mathbf{a}_2}{2\sqrt{3}}$ as shown in Fig S10(a)). Here, $\mathbf{a}_1 = a\hat{x} + \sqrt{3}a\hat{y}$, $\mathbf{a}_2 = -a\hat{x} + \sqrt{3}a\hat{y}$, and a is the lattice constant. Under these magnetic space groups, the right-handed case again preserves $\mathbf{M} = (0, 0, 0)$, whereas the left-handed case exhibits $\mathbf{M} = (0, M^y, 0)$ that constrained by $C_{2_1x}\mathcal{T}$ and $C_{2_1z}\mathcal{T}$. Consequently, the in-plane magnetization $\mathbf{M}$ and the associated magnetic torque $\boldsymbol{\tau} \propto \mathbf{M} \times \mathbf{H}$ may vanish in the right-handed chiral antiferromagnet, whereas a nonzero magnetic torque is allowed in the left-handed chiral antiferromagnet. Table S2 summarizes the in-plane magnetization and magnetic torque in response to an in-plane external magnetic field.

Focusing on the nonzero magnetization in left-handed chiral antiferromagnets, we decompose it into two contributions: $\mathbf{M} = \mathbf{M}^0 + \mathbf{M}^\mathrm{e}$, where $\mathbf{M}^0$ is the spontaneous magnetization (branch-resolved as $\mathbf{M}^0_{f,b}$ in the main text) and $\mathbf{M}^\mathrm{e}$ is the external field induced magnetization. Here, $\mathbf{M}^0$ itself depends on the external magnetic field $\mathbf{H}$. For simplicity, we set the $\mathbf{n}_\mathrm{C} = (0, 1, 0)$ and consider an external magnetic field $\mathbf{H}$ along x-direction as $\mathbf{H} = (H^x, 0, 0)$. Under near-zero-field and zero-temperature conditions, the leading-order magnetization components are given by $\mathbf{M}^0 = \chi^0(0, 1, 0)$, and $\mathbf{M}^\mathrm{e} = \chi H^x(0, 1, 0)$. Two main cases arise, corresponding to reciprocal and nonreciprocal magnetic responses:

- **Reciprocal torque response (e.g., ferromagnet).**

  In a conventional scenario, the state resulting from the forward process at zero field is the time-reversal-symmetry partner of the state from the backward process at zero field. This symmetry constraint leads to a sign change in the total magnetization, characterized by $\mathbf{M}^0 \to -\mathbf{M}^0$ while leaving χ unchanged ($\chi \to \chi$). Consequently, the z-components of the magnetic torques under forward and backward magnetic fields are given by

  $$\tau_{z,f} \sim -\chi_f(H^x)^2 - \chi^0_f H^x, \text{ and } \tau_{z,b} \sim -\chi_b(H^x)^2 + \chi^0_b H^x. \tag{S2}$$

  This torque response therefore exhibits a symmetric behavior in the hysteresis loop, expressed as $\tau_{z,f}(H^x) = \tau_{z,b}(-H^x)$.

- **Nonreciprocal torque response (this work, $\mathbf{Mn_3Ge}$).**

  When spin-orbit coupling is sufficiently strong, its interplay with magnetic orders can break the previous time-reversal-symmetry arguments. In this regime, the strong magnetic anisotropy pins the spontaneous magnetization $\mathbf{M}^0$ to a specific direction lying within a mirror plane. If the external magnetic field is applied perpendicular to this pinned $\mathbf{M}^0$, then $\mathbf{M}^0$ does not reverse sign upon field reversal. However, the hysteresis loop splits at low fields because χ changes sign ($\chi \to -\chi$) under field reversal. As a result, the forward and backward magnetic torques become

$$\tau_{z,f} \sim -\chi_f^0 H^x - \chi_f (H^x)^2, \text{ and } \tau_{z,b} \sim -\chi_b^0 H^x + \chi_b (H^x)^2. \tag{S3}$$

It gives rise to our definition of nonreciprocal torque response: $\tau_{z,f}(H^x) = -\tau_{z,b}(-H^x)$.

In real materials, the response is termed nonreciprocal when the nonreciprocal channel dominates over the reciprocal one, as discussed in the main text. Here, we propose a possible mechanism for such a response induced by the pinned $\mathbf{M}^0$, as illustrated in Fig. S10(d): the magnetization $\mathbf{M}$ tilts by different angles under forward and backward magnetic fields. Near the zero-field limit, the antiferromagnetic configuration retains the form established under a strong field. In this process, both the magnitude and the tilt angle of the magnetization differ between the two field directions. In the following, we use concrete tight-binding model calculations to demonstrate this picture.

Effective model and numerical results

To investigate the origin of anisotropic magnetization, we consider a two-dimensional antiferromagnetic kagome-lattice model featuring three p orbitals (p_x, p_y, p_z) under the spin space group $P^{3z}6/^{1}m^{2x}m^{2xy}m^{m_z}1$ (*20*), which captures the symmetry of Mn$_3$X thin films. The tight-binding Hamiltonian reads

$$\mathcal{H} = \sum_{\langle ij\rangle,\langle\tau\tau'\rangle,s} t_{ij}^{\tau\tau'} c_{i\tau s}^\dagger c_{j\tau' s} + \sum_{i,\tau,s} \mu c_{i\tau s}^\dagger c_{i\tau s} + \sum_{i,\tau,s} \Delta_{i\tau s} c_{i\tau s}^\dagger c_{i\tau s} + J \sum_{i,\tau,\langle ss'\rangle} (\mathbf{n}_i \cdot \sigma_{ss'}) c_{i\tau s}^\dagger c_{i\tau s'}, \tag{S4}$$

where i, j label atomic sites, τ denotes the orbital index, s is the spin index, and $\mathbf{n}_i$ indicates the direction of the local magnetic moment. μ is the chemical potential, and J is the strength of the local antiferromagnetic exchange. For p-orbital, the nearest-neighbor hopping amplitudes $t_{ij}^{\tau\tau'}$ can be expressed in terms of Slater–Koster integrals (*59,60*). For example, $t_{ij}^{xx} = l^2 V_{pp\sigma} + (1-l^2) V_{pp\pi}$, $t_{ij}^{xy} = lmV_{pp\sigma} - lmV_{pp\pi}$, $t_{ij}^{xz} = lnV_{pp\sigma} - lnV_{pp\pi}$, where the direction vector connecting i site to

j site is $\mathbf{R}_i - \mathbf{R}_j = (l, m, n)$, $V_{pp\sigma}$ and $V_{pp\pi}$ are the σ- and π-bond integrals, respectively. In accordance with the spin space group $P^{3z}6/^{1}m^{2x}m^{2xy}m^{m_z}1$, both the crystal-field splitting $\Delta_{i\tau s}$ and the magnetic direction $\mathbf{n}_i$ must obey the threefold rotational symmetry $\{\mathcal{U}_{3z}||C_{3z}\}$. Moreover, the vectors $\mathbf{n}_i$ are given by $\mathbf{n}_i = (\sin\theta_i, -\cos\theta_i, 0)$, with the in-plane angles satisfying $\theta_{\mathrm{A}} = \theta_{\mathrm{C}} + \kappa 2\pi/3$ and $\theta_{\mathrm{B}} = \theta_{\mathrm{A}} + \kappa 2\pi/3$. Taking the C site as a reference (the global rotation angle $\theta_{\mathrm{g}} = \theta_{\mathrm{C}}$), we have $\Delta_{\mathrm{A}\tau s} = C_{3z}^{\dagger}\Delta_{\mathrm{C}\tau s}C_{3z}$, $\Delta_{\mathrm{B}\tau s} = C_{3z}^{\dagger}\Delta_{\mathrm{A}\tau s}C_{3z}$.The chiral antiferromagnet with two different chiralities exhibits the same spin space symmetry, as described by the spin space group $P^{3z}6/^{1}m^{2x}m^{2xy}m^{m_z}1$. In the antiferromagnetic model described by this spin space group, the spin space symmetries impose that the net magnetization vanishes and forbid the asymmetric magnetic torque behavior discussed in the main text.

To generate the anisotropic magnetization, we incorporate spin–orbit coupling, whose structure depends on the antiferromagnetic order (*22, 61*), as

$$\mathcal{H}_{\mathrm{SOC}} = \sum_{i,\alpha} (\lambda_{\mathrm{SOC},\alpha} \boldsymbol{\ell}_i^{\alpha} \cdot \mathbf{L})\sigma_\alpha, \tag{S5}$$

where $\boldsymbol{\ell}_i^{\alpha}$ is the spin–orbit vector at site i, with α as the color index. The $\mathbf{L}$ the orbital angular momentum, and σ_α the Pauli matrix acting on the spin degree of freedom. In this chiral antiferromagnet, the spin–orbit vectors are given by

$$\boldsymbol{\ell}_i^{1} = (\sin\theta_i, -\cos\theta_i, 0),\ \boldsymbol{\ell}_i^{2} = (\cos\theta_i, \sin\theta_i, 0),\ \text{and}\ \boldsymbol{\ell}_i^{3} = (0, 0, 1). \tag{S6}$$

Here, spin–orbit coupling breaks the symmetries of the spin space group and leads to distinct magnetic space groups for the right-handed and left-handed chiral antiferromagnets. Based on the magnetic space groups listed in Table S2, the left-handed case exhibits higher symmetry, which typically results in lower free energy F_E. Using the band structure of $\mathcal{H} + \mathcal{H}_{\mathrm{SOC}}$, the free energy is calculated as

$$F_E = \sum_n \int_{\mathrm{BZ}} f_{E_F}(E_n) E_n(\mathbf{k}) d\mathbf{k}. \tag{S7}$$

where f_{E_F} is Fermi-Dirac distribution. Figure S10(b) presents the numerical results for F_E of the right-handed and left-handed chiral antiferromagnets. Focus on the left-handed case, the spontaneous magnetization $\mathbf{M}^0$ depends on strength of spin-orbit coupling λ_{SOC}, as shown in Fig S10(c). In figure S10, we set the parameters as follows: $V_{pp\sigma} = 1$, $V_{pp\pi} = \frac{1}{2}V_{pp\sigma}$, $\Delta_{\mathrm{C}p_x\uparrow} = \Delta_{\mathrm{C}p_x\downarrow} = 0$,

$\Delta_{\mathrm{C}p_y\uparrow} = \Delta_{\mathrm{C}p_y\downarrow} = 0.9V_{pp\sigma}$, $\Delta_{\mathrm{C}p_z\uparrow} = \Delta_{\mathrm{C}p_z\downarrow} = 1.2V_{pp\sigma}$, $J = 0.2V_{pp\sigma}$, $\lambda_{\mathrm{SOC}} = \lambda_{\mathrm{SOC},x} = \lambda_{\mathrm{SOC},y} = 2\lambda_{\mathrm{SOC},z} = 0.05V_{pp\sigma}$, $\mu = 0.27V_{pp\sigma}$.

On the other hand, we further investigate the tilting of the antiferromagnetic configuration under an external magnetic field, as described by $\mathcal{H}_B = \frac{1}{2}g\mu_B\mu_0\mathbf{H}\cdot\boldsymbol{\sigma}$. Using the band structure of $\mathcal{H} + \mathcal{H}_{\mathrm{SOC}} + \mathcal{H}_B$, we explore the interplay between spin-orbit coupling and the magnetic Zeeman field to determine the antiferromagnetic ground state, including the possibility of a spin-flop-like transition with a rotation angle of $\pi/6$. Here, we choose the magnetic field along the x-direction as $\mathbf{H} = (H^x, 0, 0)$. In Fig S10(e), we find that the global antiferromagnetic order orientation θ_{g} favors different angles for the $+H^x$ and $-H^x$ cases, as detailed below:

- **Backward case with $+H^x$ in our calculation:** The free energy reaches its global minimum when $\theta_{\mathrm{g}} = \pi/6$ or $5\pi/6$.
- **Forward case with $-H^x$ in our calculation:** The free energy reaches its global minimum when $\theta_{\mathrm{g}} = -\pi/6$ or $-5\pi/6$.

We then choose the $\theta_{\mathrm{g}} = -\pi/6$ for the forward magnetic field and $\theta_{\mathrm{g}} = \pi/6$ for the backward magnetic field. With this global rotation angle difference of $\pi/3$, the forward and backward states at zero field cannot be related by time-reversal symmetry, which thus generally allows a non-reciprocal torque response. Under this configuration, the calculated perpendicular magnetization $M^{\perp} = (0, M^y, 0)$ exhibits opposite signs (or opposite ratios), while the spontaneous magnetization remains unchanged, as shown in Fig S10(f). The resulting torque is naturally odd under field sweeps, as presented in the main text.

In the theoretical framework of spin-orbit-coupling-induced spin-space group breaking, the spin order and spin–orbit coupling are linked via rigid-body rotation. This effect gives rise to an anisotropic anomalous Hall conductivity which depending on the orientation of the antiferromagnetic order (*22, 61*), such as

$$\sigma_{ab}^{\mathrm{HE}} = [2\sqrt{3}(b_2 - b_1 - a_1) + c_1]\cos\theta_{\mathrm{g}} + c_2\cos\theta_{\mathrm{g}}\cos 2\theta_{\mathrm{g}}, \tag{S8}$$

where θ is the angle of spin order, and b_1, b_2, c_1, c_2 are constant coefficients. When the magnetic-field-driven spin order is near $\theta_{\mathrm{g}} = 0$, the Hall resistivity $\rho_{ab}^{\mathrm{HE}} = 1/\sigma_{ab}^{\mathrm{HE}}$ takes opposite values for forward and backward magnetic fields near $|\mathbf{H}| = 0$. Conversely, when the magnetic-field-driven spin order is near $\theta_{\mathrm{g}} = \pi/2$, the Hall resistivity takes the same values for forward and backward magnetic fields. This behavior is consistent with the Hall hysteresis loop.

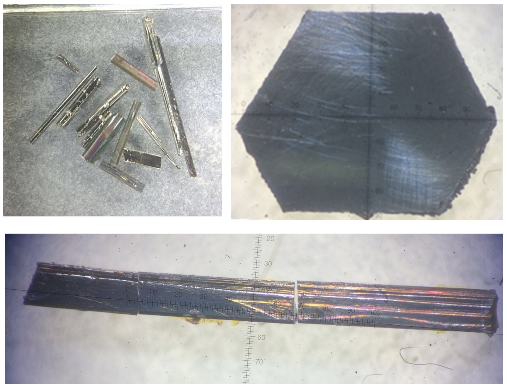

Figure S1: **The image of the As-grown Mn_3Ge single crystals.**

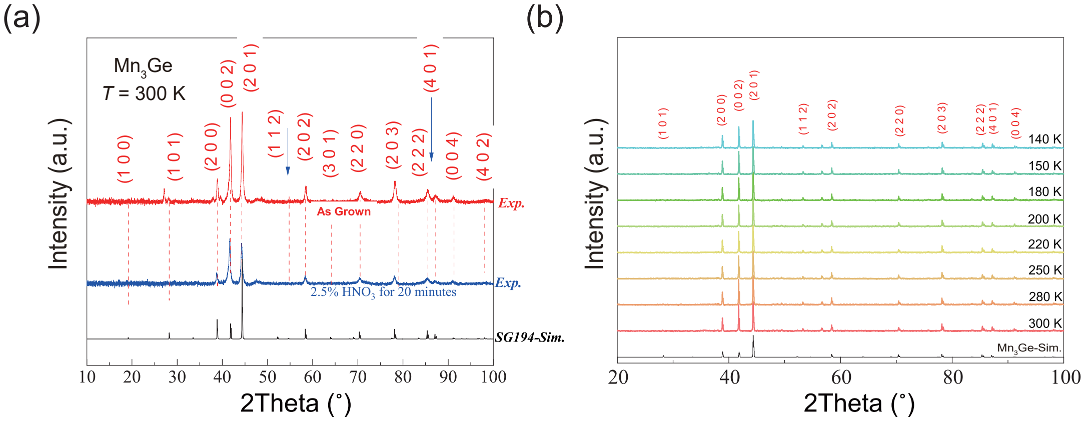

Figure S2: **Powder XRD result.** (a) Powder XRD patterns of Mn_3Ge before and after removal of residual flux using diluted nitric acid. (b) XRD patterns of Mn_3Ge powder at different temperatures.

Table S1: **Comparison of various observations between domain wall induced PHE (follow Ref. (*54, 55*)) and intrinsic PHE from nonreciprocal magnetic response.**

Physical Property	Domain wall effect	Nonreciprocal magnetic response
Onset temperature	370 K ($= T_N$)	~200 K ($\ll T_N$)
Temperature dependence	scaled by $M(T)$	irrelevant to $M(T)$
Prior field training	decrease with H_p	irrelevant to H_p
Memory effect	YES	NO
PHE sign	switchable	non-switchable

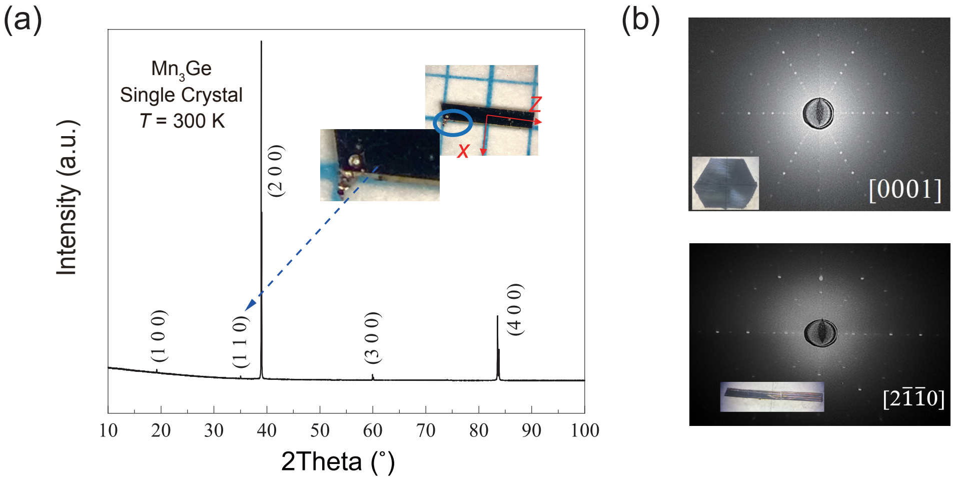

Figure S3: **Single crystal XRD result.** (a) X-ray diffraction (XRD) patterns of the Mn_3Ge single crystal surface. (b) Laue patterns of the Mn_3Ge single crystal surface.

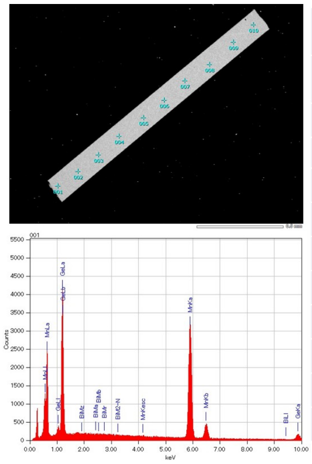

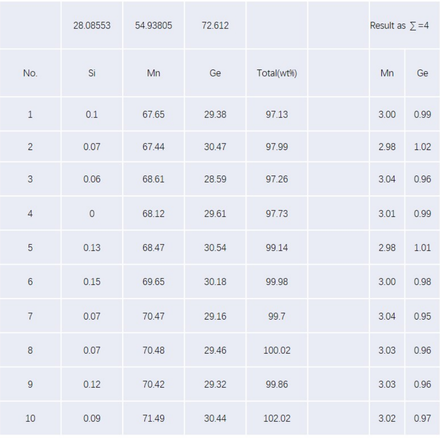

	28.08553	54.93805	72.612			Result as ∑=4	
No.	Si	Mn	Ge	Total(wt%)		Mn	Ge
1	0.1	67.65	29.38	97.13		3.00	0.99
2	0.07	67.44	30.47	97.99		2.98	1.02
3	0.06	68.61	28.59	97.26		3.04	0.96
4	0	68.12	29.61	97.73		3.01	0.99
5	0.13	68.47	30.54	99.14		2.98	1.01
6	0.15	69.65	30.18	99.98		3.00	0.98
7	0.07	70.47	29.16	99.7		3.04	0.95
8	0.07	70.48	29.46	100.02		3.03	0.96
9	0.12	70.42	29.32	99.86		3.03	0.96
10	0.09	71.49	30.44	102.02		3.02	0.97

Figure S4: **SEM/EDS of the Mn_3Ge single crystal surface.**

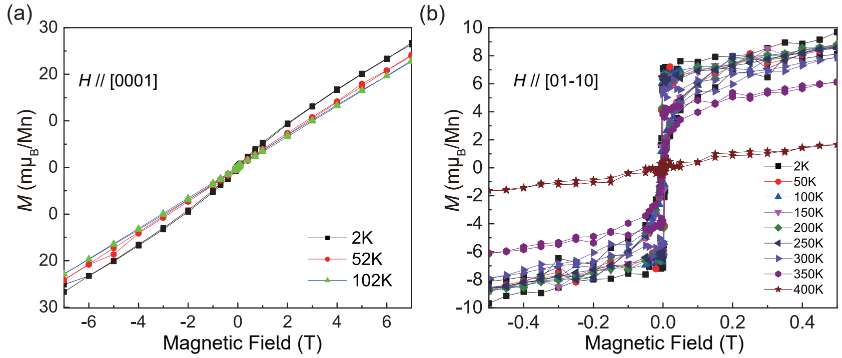

Figure S5: **Magnetization measurement.** (a) Out-plane *MH* curve of the Mn_3Ge single crystal. (b) In-plane *MH* curve of the Mn_3Ge single crystal.

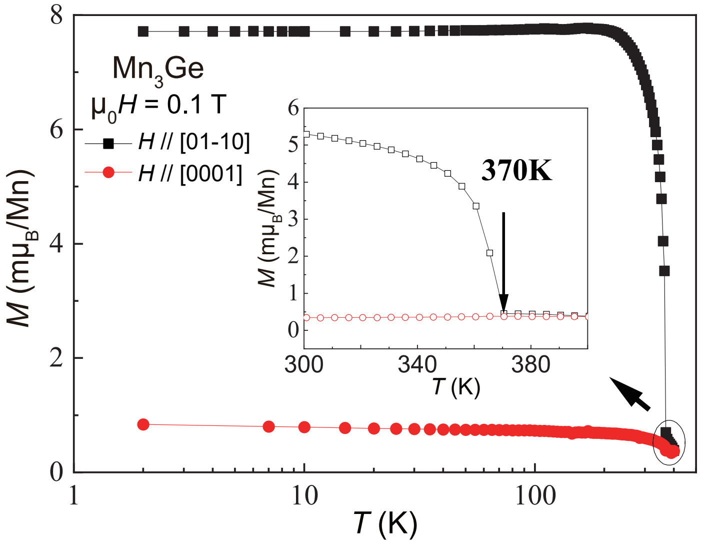

Figure S6: ***M*-*T* curve of the Mn_3Ge single crystals.**

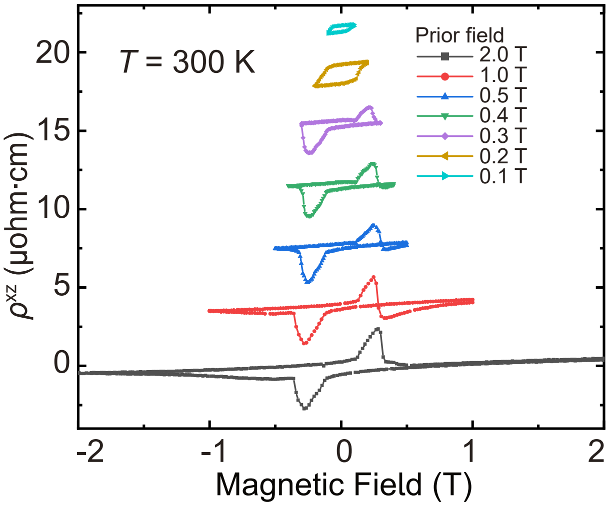

Figure S7: **The Hall measurement (ρ^{xz} with $\mathbf{H} \parallel x$) at 300 K with different strength of prior field (H_p) training.**

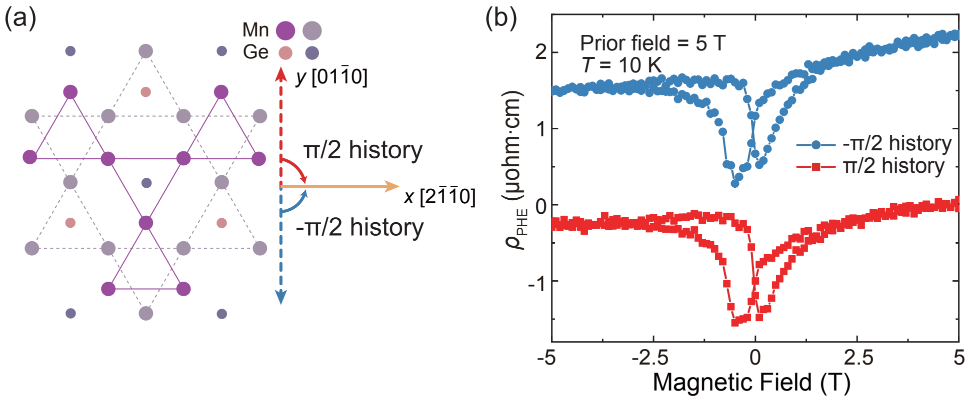

Figure S8: **Test of memory effect.** (a) Schematic diagram showing two histories of magnetic field changes. The dashed lines represent the initial magnetic-field directions, with the red and blue ones corresponding to the history states of $\pi/2$ and $-\pi/2$, respectively. The orange solid arrow indicates the final field state. After rotating the field from its initial direction to the final direction, the planar Hall measurement is performed. (b) The planar Hall measurement with 5 T prior field applied along $+y$ (red curve) or $-y$-axis (blue curve). The PHE signal shows no obvious change with the direction of H_p, indicating no memory effect. Blue curve is offset by 2 $\mu\Omega$ cm for clarity.

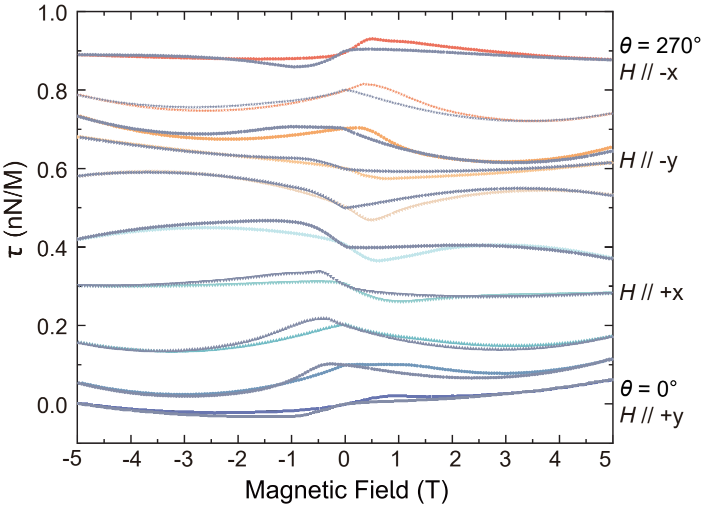

Figure S9: **Detail of torque results in different direction.** Magnetic torque results measured at 10 K with the magnetic field rotating from $\theta = 0°$ to $\theta = 270°$ (30° difference for adjacent curves). Each pair of curves was obtained for forward (colored curves) and backward (gray curves) field sweeps. Curves are offset vertically for clarity.

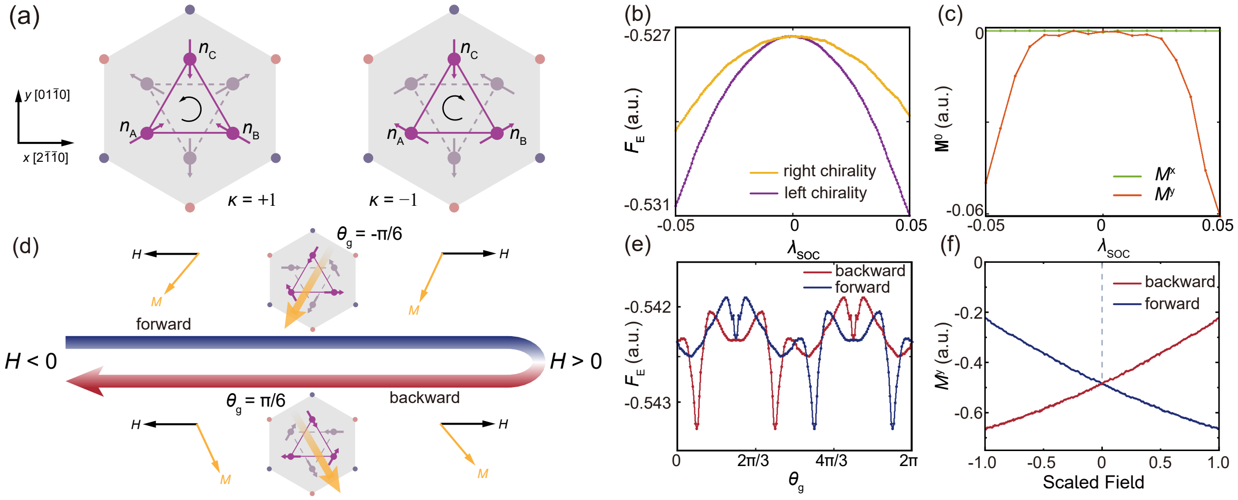

Figure S10: **Anisotropic magnetization mechanism in chiral antiferromagnets.** (a) The spin configuration with right-handed and left-handed chirality ($\kappa = \pm 1$). (b) The free-energy for right-handed and left-handed case. (c) The spin-orbit coupling induced spontaneous magnetization. (d) The schematic of spin configuration tilt mechanism. (e) The free-energy with spin order orientation θ_{C} under x-direction magnetic field H^x. (f) The magnetization hysteresis loop under magnetic field H^x.

Table S2: **Symmetry analysis.** Symmetry-allowed nonzero magnetization $\mathbf{M}$ and nonzero magnetic torque $\boldsymbol{\tau}$ for right-handed and left-handed antiferromagnetic configurations with spin–orbit coupling. The applied external magnetic field $\mathbf{H} = (H^x, H^y, 0)$ lies in the x-y plane.

Chirality	Magnetic space group	$\mathbf{M} = (M^x, M^y, M^z)$	$\boldsymbol{\tau} \propto \mathbf{M} \times \mathbf{H}$
$\kappa = +1$	$P6_3'$ (where $\mathbf{n}_\mathrm{C} \neq \pm(\mathbf{a}_1 \pm \mathbf{a}_2)$)	$\mathbf{M} = (0,0,0)$	$\boldsymbol{\tau} \propto (0,0,0)$
$\kappa = +1$	$P6_3'22'$ (where $\mathbf{n}_\mathrm{C} = \pm(\mathbf{a}_1 \pm \mathbf{a}_2)$)	$\mathbf{M} = (0,0,0)$	$\boldsymbol{\tau} \propto (0,0,0)$
$\kappa = -1$	$P2_1'$ (where $\mathbf{n}_\mathrm{C} \neq \pm(\mathbf{a}_1 \pm \mathbf{a}_2)$)	$\mathbf{M} = (M^x, M^y, 0)$	$\boldsymbol{\tau} \propto (0,0,M^xH^y - M^yH^x)$
$\kappa = -1$	$P2_1'2'2$ (where $\mathbf{n}_\mathrm{C} = \pm(\mathbf{a}_1 - \mathbf{a}_2)$)	$\mathbf{M} = (M^x, 0, 0)$	$\boldsymbol{\tau} \propto (0,0,M^xH^y)$
$\kappa = -1$	$P2_1'2'2$ (where $\mathbf{n}_\mathrm{C} = \pm(\mathbf{a}_1 + \mathbf{a}_2)$)	$\mathbf{M} = (0, M^y, 0)$	$\boldsymbol{\tau} \propto (0,0,-M^yH^x)$